THE ASTROPHYSICAL JOURNAL, 450:628–637, 1995 September 10

PHOTOEVAPORATION OF DUSTY CLOUDS NEAR ACTIVE GALACTIC NUCLEI

EDWARD A. PIER[1]
Code 665, NASA/Goddard Space Flight Center, Greenbelt, MD 20771
AND
G. MARK VOIT[2]
Department of Physics and Astronomy, The Johns Hopkins University, Baltimore, MD 21218
Received 1994 December 2; accepted 1995 March 23

ABSTRACT

We investigate the hydrodynamic and line-emitting properties of dusty clouds exposed to an active galactic nucleus (AGN) continuum. Such clouds may be found on the inner edges of the tori commonly implicated in AGN unification schemes. An X-ray–heated wind will be driven off the surface of such a cloud, eventually destroying it. Dust grains are carried along with the flow and are destroyed by sputtering as the wind heats. In smaller clouds, sputtering regulates the outflow by reducing the radiation force opposing the flow. Cloud evaporation may be fast enough to determine the location of the inner edge of the torus. However, since the evaporation time is much longer than the orbital time, clouds on eccentric orbits can penetrate well inside the inner edge of the torus. Therefore, the ionization structure of the cloud is determined only by the incipient continuum shape.

The inner faces of exposed clouds are pressurized primarily by the incident radiation. Radiation pressure on dust grains regulates how gas pressure increases with optical depth. Ionization levels decrease inward, and the bulk of the cloud is molecular and neutral. The effects of dust extinction and high density suppress the hydrogen recombination lines and the forbidden lines from C, N, and O ions below observed levels despite the high covering factor expected for the torus. However, the inner edge of the torus is a natural place for producing the iron coronal lines often seen in the spectra of AGNs (i.e., [Fe VII] λ6087, [Fe X] λ6375, [Fe XI] λ7892, and [Fe XIV] λ5303).

Subject headings: dust, extinction — galaxies: active — galaxies: Seyfert — hydrodynamics — ISM: clouds — line: formation

1. INTRODUCTION

Active galactic nuclei (AGNs) appear to be a diverse group, but their phenomenological variety probably disguises many fundamental similarities. Seyfert 1 galaxies characteristically emit strongly in the UV and X-ray bands, and their spectra exhibit permitted lines several thousand km s^{-1} broad. Seyfert 2 galaxies are weaker UV/X-ray emitters and have narrower emission lines, but several observational findings indicate that Seyfert 1 and Seyfert 2 galaxies are intrinsically similar objects seen from different aspect angles. In particular, the polarized broad emission lines from some Seyfert 2 galaxies show that dusty obscuring gas, probably arranged toroidally, partially covers the broad-line–emitting regions of these objects (Antonucci & Miller 1985; Miller & Goodrich 1990; Tran, Miller, & Kay 1992; Kay 1994).

Several other lines of evidence also indicate the presence of these obscuring tori. Notably, along unobscured directions, an active nucleus irradiates the interstellar medium of its host galaxy, producing an ionized cone of gas with the nucleus at its vertex. These ionization cones are observed in many Seyfert galaxies (e.g., Wilson, Ward, & Haniff 1988; Pogge 1988, 1989; Evans et al. 1991; Macchetto et al. 1994; Mulchaey 1994). Both type 1 and type 2 Seyfert galaxies are strong mid-infrared ($\sim 10\ \mu$m) emitters. This emission is probably nuclear radiation reprocessed by the torus. The fact that nearly all AGNs have similar strong infrared emission suggests that obscuring tori may be ubiquitous; thus, these tori have become a cornerstone of the so-called unified theories of AGNs. For more on AGN unification and observational evidence for tori, see Antonucci (1993) and Ward (1994).

At least half of all Seyfert galaxies are of type 2 (Lawrence 1991), so a typical AGN torus must cover a large solid angle around the nucleus. Thermal infrared continuum formation in AGNs also requires a large covering factor of dusty obscuring gas for a sufficient proportion of the emitted ultraviolet flux to be reprocessed into the infrared band (Sanders et al. 1989; Edelson, Malkan, & Rieke 1987; Pier & Krolik 1993). The covering factors implied by the infrared luminosities of AGNs are consistent with those inferred from the opening angles of their ionization cones (Storchi-Bergmann, Mulchaey, & Wilson 1992; Schmitt, Storchi-Bergmann, & Baldwin 1994). Since the torus intercepts an ionizing luminosity several times greater than that absorbed in the broad-line region, one might expect its recombination-line output to be enormous. However, if the ionization levels at the surface of the torus are very high, the opacity of the gas above the Lyman limit is reduced, and dust can absorb most of the incident ionizing radiation, reducing the production of emission lines (Voit 1992; Netzer & Laor 1993).

Supporting such a geometrically thick torus requires the obscuring material to be clumped into discrete clouds whose random velocities are of order their orbital velocities (Krolik & Begelman 1988). Collisions between clouds in the differentially rotating torus conduct angular momentum outward and mass inward, just as in accretion disks and planetary rings. To sustain these tori, molecular material must continually be

[1] NAS-NRC Research Associate.
[2] Hubble Fellow.

resupplied at the outer edge. On the inner edge of the torus, the UV/X-ray flux from the AGN can heat, ionize, and evaporate gas from the exposed surfaces of the obscuring clouds. The evaporated material then either accretes onto the central engine or flows out the hole of the torus in a Compton-heated wind (Krolik & Begelman 1986; Balsara & Krolik 1993). In a steady state, cloud evaporation at the inner edge of the torus must somehow balance the supply of molecular material at the outer edge (Krolik & Begelman 1988).

This paper investigates the evaporation of molecular clouds by intense UV/X-ray radiation in order to determine evaporation rates and emission-line fluxes at the inner edges of AGN-obscuring tori. We assume that the clouds are pressurized both by radiation pressure on dust grains and by the Compton-heated wind. Section 2 describes the structure of irradiated clouds and identifies the parameters that govern cloud evaporation. Section 3 evaluates the hydrodynamic wind equations analytically. We show that radiation pressure confines the optically thick portions of the clouds, that winds arise only where the optical depth is low, and that radiation pressure suppresses evaporation if sputtering of dust is ineffective. In § 4 we construct numerical models of X-ray–heated winds from dusty clouds in order to quantify how dust destruction regulates evaporation rates. In § 5 we model the emission-line spectra from radiation pressure–confined dusty clouds and compare these line fluxes to observations. Section 6 summarizes our results.

2. CLOUD AND WIND PROPERTIES

Most models of clouds in the vicinity of AGNs have assumed that a hot pressurizing medium confines these clouds and regulates their ionization levels (e.g., Krolik, McKee, & Tarter 1981; Ferland & Osterbrock 1986). By way of contrast, this paper studies the structure of AGN-irradiated clouds with a zero-pressure boundary condition at infinity. The clouds we model here are confined primarily by radiation pressure on dust grains at the cloud surface and secondarily by the back-reaction of an evaporative wind driven by X-ray heating. The internal ionization structure of a cloud is therefore governed only by the incident spectral flux and the chemical composition of the cloud. This section outlines the general characteristics of these X-ray–irradiated clouds and the winds surrounding them.

2.1. *Structure*

Clouds a few tenths of a parsec from a 10^{44} ergs s^{-1} AGN receive a radiation flux $\sim 10^7$ ergs cm^{-2} s^{-1}. This corresponds to an effective temperature $\simeq 650$ K, consistent with the value for the inner edge of the torus suggested by infrared radiative transfer models (Pier & Krolik 1993). The νF_ν spectrum incident on the clouds peaks in the ultraviolet but carries similar amounts of power in the infrared and X-ray bands. The average energy per ionizing photon in rydbergs is thus $\bar{E}_{\rm Ryd} \gtrsim 1$. Here we take the ionizing energy flux to be $F_{\rm ion} = (10^7$ ergs cm^{-2} s$^{-1})F_7$, giving an ionizing photon flux $F_{\rm ph} \simeq (4.6 \times 10^{17}$ cm^{-2} s$^{-1})F_7 \bar{E}_{\rm Ryd}^{-1}$. The hydrogen ionization timescale $t_i \sim (0.35$ s$)\ F_7^{-1} \bar{E}_{\rm Ryd}$ is much shorter than most others in these clouds.

Ionization and thermal balance within AGN-irradiated clouds depends on an ionization parameter, such as $\Xi \equiv F_{\rm ion}/cP_g$ (where P_g is the gas pressure) or U, equal to the density of ionizing photons divided by the density of hydrogen nuclei, $n_{\rm H}$. The parameter U is handy for evaluating ionization balance in a static medium, but in dynamical problems, Ξ is often more useful. In a gas at temperature $T = (10^4\ {\rm K})T_4$ with χ_p particles per H nucleus, $\Xi = (16\bar{E}_{\rm Ryd}\, \chi_p^{-1} T_4^{-1})U$.

Line cooling in gas heated by photoionizing UV radiation alone keeps the equilibrium gas temperature $T_{\rm eq}$ near 10^4 K (Krolik et al. 1981; see Fig. 1). X-rays can destroy the coolants that govern this thermostat. When Ξ exceeds a critical value $\Xi_{\rm cr}$, which depends on the ratio of X-ray to UV photons in the AGN spectrum, heating balances cooling only at the Compton equilibrium temperature $T_{\rm C}$. The suddenness of the transition from $T_{\rm eq} \sim 10^4$ K to $T_{\rm C}$ depends on the AGN spectral shape. In this paper, we will assume that the AGN spectrum is hard enough (i.e., X-ray flux at least $\sim 10\%$ of UV flux) to produce a two-phase medium at $\Xi \lesssim \Xi_{\rm cr}$, so that the transition is abrupt. When this is the case, $\Xi_{\rm cr} \sim 10$ (Krolik et al. 1981).

Since P_g goes to zero at infinity, Ξ increases outward through the cloud. Above the point where $\Xi = \Xi_{\rm cr}$, X-ray heating drives a themal wind. Therefore, by definition, $\Xi = \Xi_{\rm cr}$ at the cloud surface. Since $\Xi_{\rm cr} > 1$, radiation pressure confines an optically thick cloud more effectively than does the back-reaction of the wind. In this paper we assume self-gravity is negligible (see § 2.2), in which case P_g within the cloud depends primarily on the absorption of the incident radiation field.

Figure 2 shows a schematic picture of the cloud and wind.

2.2. *Below the Cloud Surface*

A cloud with a dust-to-gas ratio χ_d times the Galactic value (1:100 by mass; Spitzer 1978) becomes optically thick in the ultraviolet at a hydrogen column density $N_d \approx (6 \times 10^{20}$ cm$^{-2})\chi_d^{-1}$ (Draine & Lee 1984). A photoionized cloud at 10^4 K becomes optically thick in the Lyman continuum at a column of $N_i \approx (10^{23}$ cm$^{-2})U$ (Fig. 3). Thus, in dusty clouds ($\chi_d \sim 1$), the gas dominates the UV opacity only where $\Xi < 0.1$. Since the cloud is confined primarily by radiation pressure, Ξ is this low only at substantial optical depth, where most of the UV

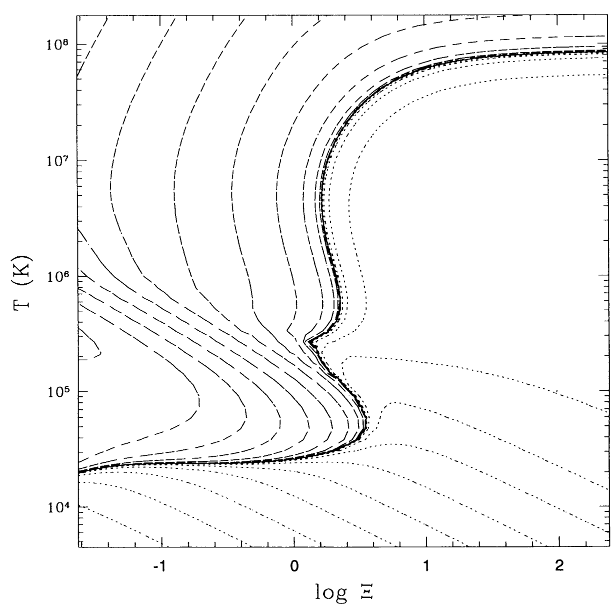

FIG. 1.—Heating rate as a function of Ξ and T. The dashed lines represent contours of net heating, and the dotted lines represent contours of net cooling. The contours are logarithmic with two per decade. The thermal equilibrium curve is represented by a solid line.

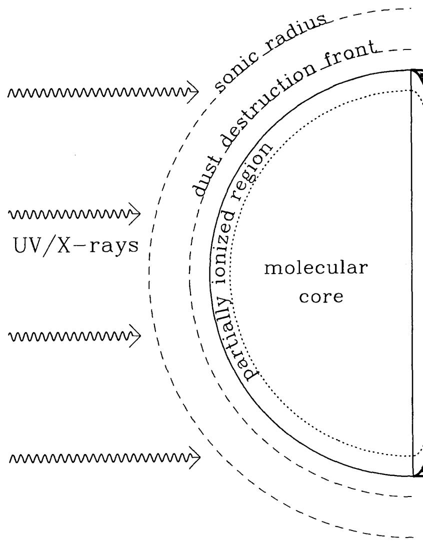

FIG. 2.—Schematic picture of the cloud and wind, not drawn to scale

photons have already been absorbed. X-rays easily penetrate to this layer because the X-ray opacity of dust is only 10^{-1} to 10^{-3} times its UV opacity. In the X-rays, dust opacity is comparable to gas opacity, unless the metals in the gas are completely ionized (Morrison & McCammon 1983).

At a UV dust optical depth $\tau_d > 1$ into the cloud, $P_g \sim F_{\rm ion}/c = (3.3 \times 10^{-4}$ ergs cm$^{-3})F_7$ and $n_{\rm H} \sim (1.1 \times 10^8$ cm$^{-3})F_7 T_4^{-1}$. The thickness of the layer with $\tau_d \sim 1$ is therefore $\sim(6 \times 10^{12}$ cm$)F_7^{-1} T_4 \chi_d^{-1}$. When $\tau_d > 10$–30, the gas becomes predominantly molecular with an equilibrium temperature $\sim(10^3$ K$)T_{\rm mol3}$ (Krolik & Lepp 1989; Neufeld, Maloney, & Conger 1994) and density $n_{\rm H} \simeq (4.0 \times 10^9$ cm$^{-3})F_7 T_{\rm mol3}^{-1}$. The Jeans length in this gas is $\sim(1.3 \times 10^{16}$ cm$)F_7^{-1/2} T_{\rm mol3}$, so we scale the cloud radius as $r_{\rm cl} = (10^{16}$ cm$)r_{16}$. The surface layer with $\tau_d < 10$ is comparatively very thin and essentially plane-parallel. Molecular gas dominates the cloud mass,

$$M = 20\xi r_{16}^3 F_7\, T_{\rm mol3}^{-1} M_\odot\,, \qquad (1)$$

where ξ = cloud volume/$(4/3)\pi r_{\rm cl}^3$. The surface gravity of the cloud is $(2.6 \times 10^{-5}$ cm s$^{-2})r_{16} F_7 T_{\rm mol3}$, while the radiation pressure acceleration on the cloud surface is $(0.25$ cm s$^{-2})F_7 \chi_d$. Therefore, we may neglect the influence of cloud gravity on wind dynamics. Dusty clouds with $r_{16} \sim 1$ and $n_{\rm H} \sim 10^9$ cm^{-3} are optically thick from the far-infrared through the X-ray band and have extremely large optical thicknesses in the ultraviolet.

2.3. *X-Ray–Heated Wind*

The heating rate per unit mass in gas with $\Xi > \Xi_{\rm cr}$ is of order the Compton heating rate

$$H_{\rm C} = \frac{4kT_{\rm C}}{m_e c^2}\,\sigma_{\rm T} F_{\rm tot}\,\frac{n_e}{\rho}\,, \qquad (2)$$

where $F_{\rm tot} \sim F_{\rm ion}$ is the total radiative energy flux, $\sigma_{\rm T}$ is the Thomson cross section, m_e is the electron mass, n_e is the electron number density, and ρ is the mass density. When the Compton temperature is $T_{\rm C} = (10^8$ K$)T_{\rm C8}$, we have $H_{\rm C} \approx (2.3 \times 10^5$ ergs s^{-1} g$^{-1})T_{\rm C8} F_7$. The time needed to attain $T_{\rm C}$ is $t_{\rm C} \sim (10^{11}$ s$)F_7^{-1}$. Combining the Compton heating rate and the cloud radius gives a flow timescale for the exterior wind $t_f = r_{\rm cl}^{2/3} H_{\rm C}^{-1/3} = (7.6 \times 10^8$ s$)r_{16}^{2/3} T_{\rm C8}^{-1/3} F_7^{-1/3}$ and a corresponding characteristic velocity $v_f = r_{\rm cl}/t_f = (1.3 \times 10^7$ cm s$^{-1})r_{16}^{1/3} T_{\rm C8}^{1/3} F_7^{1/3}$ and temperature $T_f = m_{\rm H} v_f^2/k = (2.1 \times 10^6$ K$)r_{16}^{2/3} T_{\rm C8}^{2/3} F_7^{2/3}$. In § 3 we demonstrate that v_f is approximately the velocity at the sonic point in an X-ray–heated wind, which occurs at a distance $\sim r_{\rm cl}$ beyond the cloud surface. From the cloud surface to the sonic point $P_g \sim F_{\rm ion}/\Xi_{\rm cr} c$, so at temperature T_f, we have $n_{\rm H} \sim (5.1 \times 10^5$ cm$^{-3})$ $F_7^{1/3} T_{\rm C8}^{-2/3} r_{16}^{-2/3} \Xi_{\rm cr}^{-1}$. The column density of the subsonic segment of the wind is $\sim(5 \times 10^{21}$ cm$^{-2})F_7^{1/3} T_{\rm C8}^{-2/3} r_{16}^{1/3} \Xi_{\rm cr}^{-1}$ and $\tau_d/\chi_d \sim 1$, for $\Xi_{\rm cr} \sim 10$. For a more detailed analysis of Compton-heated winds, see Begelman, McKee, & Shields (1983).

The radiation force on a dust grain is $F_{\rm tot}\,\sigma_{\rm rad}/c$, where $\sigma_{\rm rad}$ is the frequency-averaged cross section to photon absorption of the grain. The drag force on a grain moving through a gas with velocity $v_{\rm drift}$ is $\sim P_g\,\sigma_{\rm col}\, v_{\rm drift}/a$, where $\sigma_{\rm col}$ is the cross section to interactions with protons and a is the sound speed in the gas. For uncharged grains $\sigma_{\rm rad} \sim \sigma_{\rm col}$. However, Coulomb effects enhance $\sigma_{\rm col}$ by a factor ϕ^2, where ϕ is the potential energy of an electron at the grain surface divided by kT (Draine & Salpeter 1979). Since $v_{\rm drift}/a \sim \Xi\phi^2$, grains will be well coupled to the gas when $\phi \gg \Xi^{1/2} \sim$ a few. Grains capture electrons at a rate $\sim n_e\, a(m_{\rm H}/m_e)^{1/2}(1 + \phi)$ per unit surface area when $\phi > 0$. Photons eject electrons from grains at the rate $F_{\rm ph}\, Y$, where $Y \sim 0.1$ is the photoelectric yield (Draine & Salpeter 1979). Therefore, $\phi \sim 10\Xi\bar{E}_{\rm Ryd}^{-1} T_4$ is easily large enough to couple the dust grains to the gas.

Radiation pressure on dust grains can potentially suppress the wind. Let $\mathscr{F}$ be the radiation force per unit mass. Gas approaching the sonic point does work against radiation pressure at a rate $v_f \mathscr{F}$ while receiving energy from the radiation

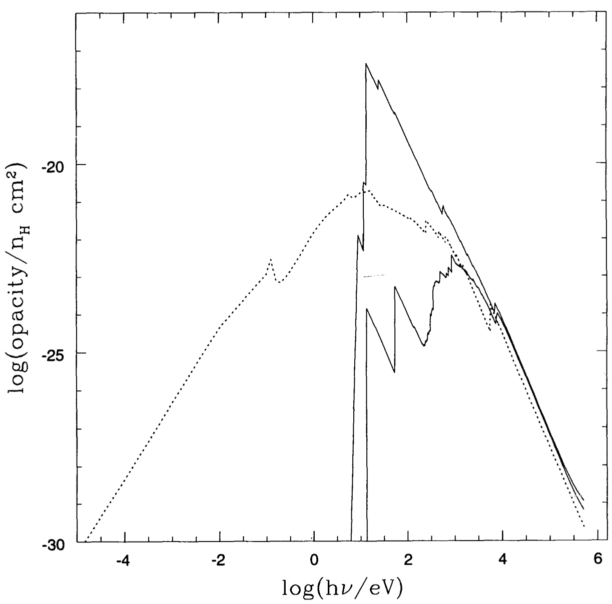

FIG. 3.—Dust and gas opacity. The dotted line represents the dust opacity curve adopted in this paper from Draine & Lee (1984) and Laor & Draine (1993). The solid curves represent the bound-free opacity of neutral gas (*upper curve*) and highly ionized gas with $\Xi \lesssim \Xi_{\rm cr}$ (*lower curve*).

field at the rate H_C. As long as $H_C \gg v_f \mathscr{F}$, radiation forces can be neglected. This condition is satisfied when

$$\bar{\sigma} \ll \frac{4kT_C}{m_e c^2} \frac{c}{v_f} \frac{n_e}{n_H} \sigma_T , \quad (3)$$

where $\bar{\sigma}$ is the spectrally weighted average cross section per H atom. Since AGNs radiate most strongly in the UV where $\bar{\sigma} \sim 10^{-21} \chi_d$ cm^{-2} (Draine & Lee 1984), we can neglect $\mathscr{F}$ when $\chi_d \ll 0.1 r_{16}^{-1/3} T_{C8}^{2/3} F_7^{-1/3}$ and the wind is optically thin. Note that if $\chi_d \sim 1$ at the sonic point, dust can strongly affect and even stifle the wind (see § 3). However, gas hotter than $\sim 10^6$ K can sputter away dust grains a_μ microns in size in $(6 \times 10^{13}$ s cm$^3)n_H^{-1} a_\mu$ (Draine & Salpeter 1979). Grains smaller than 0.1 μm disappear in a time $t_d \sim (3 \times 10^6$ s$)F_7^{-1/3} T_{C8}^{2/3} r_{16}^{2/3} \Xi_{cr}^{-1}$, much less than the flow time. At temperatures below 10^6 K the sputtering rate drops rapidly because only gas particles in the tail of the Maxwellian distribution can dislodge atoms from grains. Thus, the effects of radiation pressure on the wind are mitigated by sputtering when $r_{16} \gg 0.3 T_{C8}^{-1} F_7^{-1}$ and $T_f \gg 10^6$ K but can be severe when $r_{16} \lesssim 0.3 T_{C8}^{-1} F_7^{-1}$ and $T_f \lesssim 10^6$ K.

When X-ray–heated winds escape freely, they transport an energy flux $\sim v_f F_{\rm ion}/\Xi_{cr} c$ in a mass flow with

$$\dot{M} \sim \pi r_{cl}^2 \frac{F_{\rm ion}}{v_f \Xi_{cr} c}$$
$$\sim 1.3 \times 10^{-5} F_7^{2/3} T_{C8}^{2/3} r_{16}^{5/3} \; M_\odot \text{ yr}^{-1} . \quad (4)$$

Clouds of this kind evaporate in $M/\dot{M} \sim 10^6 r_{16}^{4/3} F_7^{1/3} T_{\rm mol3}^{-1} T_{C8}^{-2/3}$ yr.

3. ANALYTIC EVALUATION

To simplify our analysis of cloud-wind structure, we assume symmetric steady state one-dimensional flow embedded in $D + 1$ dimensions. The values $D = 0$, 1, and 2 correspond to plane-parallel, cylindrically symmetric, and spherically symmetric cases, respectively. Although the short flow times indicate that winds can achieve a steady state, winds irradiated by the parallel beam from an AGN will not be spherically symmetric. Since the wind is optically thin, the heating rate in regions not blocked by the cloud itself does not depend on the incidence angle of the radiation. However, radiation pressure forces do depend on this angle. Therefore, our analysis does not apply in regions that cannot be considered plane-parallel when radiation force terms in the wind equations approach the heating terms. We show below that the symmetric models themselves also become problematic when radiation forces are important.

The equations for symmetric steady state one-dimensional flow in $D + 1$ dimensions of a gas with adiabatic index γ can be written

$$\frac{r}{\rho v} \frac{d}{dr} \rho v = -D , \quad (5)$$

$$\rho v \frac{dv}{dr} + \frac{dP_g}{dr} = \mathscr{F} \rho , \quad (6)$$

$$\rho v \frac{d}{dr} \left(\frac{1}{\gamma - 1} \frac{P_g}{\rho} \right) - \frac{P_g v}{\rho} \frac{d\rho}{dr} = H\rho , \quad (7)$$

where r is the radial coordinate, v is the radial velocity, H is the net heating rate per unit mass, and $\mathscr{F}$ is the net force per unit mass. Since the self-gravity of the cloud is negligible, $\mathscr{F}$ is essentially the radiation force. If we define the adiabatic sound speed $a \equiv (\gamma P_g/\rho)^{1/2}$, we can write the wind equations as

$$(a^2 - v^2) \frac{d \ln v}{d \ln r} = (\gamma - 1) \frac{Hr}{v} - \mathscr{F} r - Da^2 , \quad (8)$$

$$(a^2 - v^2) \frac{d \ln a}{d \ln r} = \frac{\gamma - 1}{2} \left[\left(1 - \gamma \frac{v^2}{a^2} \right) \frac{Hr}{v} + \mathscr{F} r + Dv^2 \right] . \quad (9)$$

Wind solutions with zero pressure at $r \to \infty$ must pass through a sonic point where $v = a$ and $(\gamma - 1)Hr/v - \mathscr{F} r = Da^2$ (Bondi 1952). Note that $\mathscr{F} < 0$ at the front of the cloud because radiation forces there oppose the flow.

Let us assume H is constant and that $\mathscr{F} r$ can be neglected. At first, $a \gg v$ and $a \propto v^{1/2}$. A wind that starts at $r = r_{cl}$ and accelerates to a velocity v_s at the sonic point r_s follows the approximate solution $v \approx [2(\gamma - 1)Hv_s^{-1}(r - r_{cl})]^{1/2}$ and $a \approx [2(\gamma - 1)Hv_s(r - r_{cl})]^{1/4}$.The necessary conditions at the sonic point imply $r_s \approx r_{cl}/[1 - 1/(2D)]$ and $v_s \approx [2(\gamma - 1)Hr_{cl}/(2D - 1)]^{1/3}$. Beyond the sonic point, the wind can continue to heat and accelerate as long as a remains nearly as large as v and

$$\frac{a^2}{v^2} < \gamma - D \frac{a^2 v}{Hr} < 1 . \quad (10)$$

While both these conditions hold, $a \sim v \propto r^{1/3}$ for constant H.

A nonzero radiation force can suppress the flow. Applying L'Hôpital's rule to equations (8) and (9) at the sonic point gives

$$A\left(\frac{dv}{dr}\right)^2 + B\left(\frac{dv}{dr}\right) + C = 0 , \quad (11)$$

where

$$A = -(\gamma + 1)a , \quad (12)$$

$$B = (\gamma - 1)\left[2\mathscr{F} - (\gamma - 3) \frac{H}{a} \right] , \quad (13)$$

$$C = \frac{1}{aD} \left[(\gamma - 1) \frac{H}{a} - \mathscr{F} \right] \left\{ (\gamma - 1) \frac{H}{a} \frac{d \ln H}{d \ln r} + \mathscr{F} \frac{d \ln |\mathscr{F}|}{d \ln r} - [D(\gamma - 1) + 1] \left[(\gamma - 1) \frac{H}{a} - \mathscr{F} \right] + D\gamma(\gamma - 1) \frac{H}{a} \right\} . \quad (14)$$

A sonic point is possible only if $B^2 - 4AC > 0$ so that

$$\frac{d \ln |\mathscr{F}|}{d \ln r} < -2D \frac{\gamma - 1}{\gamma + 1} - 1 + (\gamma - 1) \frac{H}{aF} \left(D \frac{\gamma - 3}{\gamma + 1} + 1 \right) + \frac{D}{4} (\gamma + 1)(\gamma - 1)^2 \frac{(H/a\mathscr{F})^2}{1 - (\gamma - 1)H/a\mathscr{F}} - (\gamma - 1) \frac{H}{a\mathscr{F}} \frac{d \ln H}{d \ln r} . \quad (15)$$

When $D = 2$, $\gamma = 5/3$, and $H =$ const,

$$\frac{d \ln |\mathscr{F}|}{d \ln r} < -2 + \frac{16}{27} \frac{(H/a\mathscr{F})^2}{1 - (2/3)(H/a\mathscr{F})} . \quad (16)$$

In an adiabatic wind ($H = 0$), a sonic point can occur only if $|\mathscr{F}|$ is dropping rapidly ($d \ln |\mathscr{F}|/d \ln r \leq -2$). Heating makes this requirement less stringent, and a sonic point is allowed even for constant $\mathscr{F}$ when $H/a\mathscr{F} \leq -3.3$. Note that since the radiation force acts primarily on dust grains, $d\ln|\mathscr{F}|/d\ln r = d\ln \chi_d/d\ln r$.

Just above the surface of the cloud, v is small, and $H \gg -\mathscr{F}v$, so heated gas flows radially outward from the cloud surface. If this condition holds past the sonic point, our assumption of radial symmetry is adequate, and the flow from the cloud is evaporative. However, if sputtering does not reduce $|\mathscr{F}|$, $-\mathscr{F}v$ can grow large enough to suppress the thermal outflow toward the radiation source and to propel the initially radial flow around the edges of the cloud and away from the radiation source. In § 4 we present one-dimensional numerical models which demonstrate how sputtering and cloud size combine to regulate the nature of X-ray–heated winds from clouds. We will not attempt to model the two-dimensional ablation flows that occur when $-\mathscr{F}v$ dominates the dynamics.

Below the surface of the cloud, where $\Xi < \Xi_{cr}$ and $v \ll v_f$, departures from the equilibrium temperature are quickly corrected. Away from thermal equilibrium, $|H| \simeq 10H_C$, and material out of thermal balance approaches equilibrium over a characteristic distance $\Delta r = r/(d\ln a/d\ln r)$. From equation (9), $\Delta r \ll r$ below the surface of the cloud. Since the layer where $\tau_d \sim 1$ is plane-parallel and highly subsonic, the gas is also close to hydrostatic equilibrium, so that $dP_g/dr = \mathscr{F}\rho$ and $dP_g/dF_{tot} = -1/c$. The opacity of this layer depends only on its chemical composition, including dust, and the incident spectral flux. Thus, the structure of this layer and its emission-line spectrum also depend solely on these quantities. In § 5 we construct detailed models for AGN-irradiated clouds based on these principles.

4. NUMERICAL MODEL—WIND

4.1. *Computational Method*

The numerical calculations described in this section investigate more fully the structure of X-ray–heated winds from dusty evaporating clouds. We assume a spherically symmetric ($D = 2$) steady state wind illuminated from the outside by a flux $F_\nu = F_\nu^0 e^{-\tau_\nu}$, where F_ν^0 is the unattenuated nuclear flux and τ_ν is the optical depth into the wind. Our adopted F_ν^0 is a broken power-law representation of a typical AGN continuum. The $F_\nu \propto \nu^\alpha$ spectral index is -1 between 10^{-3} and 1 ryd, -1.5 between 1 and 30 ryd, -0.7 between 30 and 10^4 ryd, and -1.5 between 10^4 ryd and 511 keV. For this spectral shape, $T_{C8} = 0.86$ and $F_{ion}/F_{tot} = 0.22$. The radiation flux is directed radially inward, but because actual irradiating beams are plane-parallel, we do not include any geometric dilution or convergence of the radiation field.

We include Compton heating and cooling, free-free cooling, photoionization heating, and collisional line cooling in calculating H. We simplify the calculation of the last two rates by considering only the contributions made by oxygen ions. In the region of interest here, the total heating rates calculated this way were found to be within a factor of order unity of those produced by Timothy Kallman's much more detailed photoionization code, XSTAR (Kallman & Krolik 1993).

The dust opacity from infrared through X-rays, taken from the calculations of Laor & Draine (1993) and Draine & Lee (1984), corresponds to a Mathis, Rumpl, & Nordsieck (1977) distribution of grain sizes (Fig. 3). We adopt the grain sputtering rate calculated by Draine & Salpeter (1979) and assume a characteristic grain radius of 0.01 μm. This radius is reasonable since $\sim$0.01 μm grains dominate the dust opacity in the UV where radiation couples most strongly to the dust. We assume $v_{drift} = 0$, ignore evolution of the grain size distribution through the flow, and ignore the opacity of the gas.

The wind equations can be made nondimensional by scaling r by the Compton heating length $l_C = a_C^3/H_C$, where a_C is the sound speed at the Compton temperature of the unobscured radiation field. Note $a_C = 1.5 \times 10^8 T_{C8}^{1/2}$ cm s^{-1} so $l_C = (1.48 \times 10^{19}\ \mathrm{cm}) T_{C8}^{1/2} F_7^{-1}(F_{ion}/F_{tot})$. Equations (8) and (9) become

$$(\hat{a}^2 - \hat{v}^2)\frac{d\ln\hat{v}}{d\ln\hat{r}} = \frac{2}{3}\left(\frac{H}{H_C}\right)\frac{\hat{r}}{\hat{v}} - \left(\frac{\mathscr{F}a_C}{H_C}\right)\hat{r} - 2\hat{a}^2\,, \quad (17)$$

$$(\hat{a}^2 - \hat{v}^2)\frac{d\ln\hat{a}}{d\ln\hat{r}} = \frac{1}{3}\left[\left(1 - \frac{5}{3}\frac{\hat{v}^2}{\hat{a}^2}\right)\left(\frac{H}{H_C}\right)\frac{\hat{r}}{\hat{v}} + \left(\frac{\mathscr{F}a_C}{H_C}\right)\hat{r} + 2\hat{v}^2\right]\,, \quad (18)$$

where we have taken $\gamma = 5/3$ and $D = 2$. We will consistently use the caret symbol to denote dimensionless quantities which have been appropriately scaled by l_C or a_C. Since the radiation force acts primarily through dust grains,

$$\frac{\mathscr{F}a_C}{H_C} = -31.2\chi_d\left(\frac{T_{C8}}{0.86}\right)^{-1/2}\left(\frac{1}{0.17\kappa_1 F_{tot}}\int_0^\infty \kappa_\nu F_\nu\, d\nu\right)\,, \quad (19)$$

where κ_ν and κ_1 are the dust opacity as a function of frequency and at the Lyman edge, respectively. We have scaled T_{C8} and the frequency integral to their values when $F_\nu = F_\nu^0$. If we define $\Xi^0 = F_{tot}/(1.4cn_H m_H a_C^2)$, the continuity equation (5) becomes

$$\frac{\hat{v}\hat{r}^2}{\Xi^0} = \mathrm{const}\,. \quad (20)$$

The dust optical depth at the Lyman edge is determined by

$$\frac{d\tau_d}{d\hat{r}} = -\sigma_d\chi_d n_H l_C = -180.1\left(\frac{T_{C8}}{0.86}\right)^{-1/2}\frac{\chi_d(\hat{r})}{\Xi^0}\,, \quad (21)$$

where $\sigma_d = 1.79 \times 10^{-21}$ cm^{-2} is the dust cross section per hydrogen nucleus at the Lyman edge. The destruction of dust grains is governed by

$$\frac{d\chi_d}{d\hat{r}} = -1.81 \times 10^{-12}\frac{\chi_d n_H l_C}{v} \times\left\{1 - \exp\left[-\left(\frac{a}{1.5 \times 10^7\ \mathrm{cm\ s^{-1}}}\right)^6\right]\right\}\mathrm{cm^3\ s^{-1}} \quad (22)$$

$$= -1258.8\left(\frac{T_{C8}}{0.86}\right)^{-1/2}\frac{\chi_d}{\Xi^0\hat{v}}\left\{1 - \exp\left[-\left(\frac{\hat{a}}{0.1}\right)^6\right]\right\}\,. \quad (23)$$

Equations (22) and (23) approximate the temperature dependence of the sputtering rates found by Draine & Salpeter (1979) as $\propto T^3$ for $T \ll 10^6$ and constant for $T \gg 10^6$ K.

Equations (17)–(23) must satisfy several boundary conditions: at infinity $\tau_d \to 0$; Ξ^0 and $\hat{a}$ are fixed at the surface of the cloud; $\hat{v}$ is fixed by the requirement that the solution pass through the sonic point; and we consider only dusty clouds with $\chi_d = 1$ near the surface of the cloud. This leaves only one free parameter which we take to be the dimensionless radius of the cloud surface, $\hat{r}_{cl}$.

Equations (17)–(23) were solved by a shooting method. An initial guess of values of $\hat{r}$, Ξ^0, $\hat{a}$, $\hat{v}$, and τ_d is chosen at an arbitrary point just below the surface of the cloud. Equations (17)–(23) are then integrated outward. Inside the cloud, the gas approaches its thermal equilibrium temperature over a length scale much shorter than the length scale of the flow (see § 3). Thus, the trial solution very quickly approaches thermal equilibrium regardless of the initial guess of the values of Ξ^0 and $\hat{a}$. However, the equations are stiff here, and an implicit differencing scheme must be used to integrate them.

The integration continues out through the surface of the cloud and on to the point where either $\hat{v} = \hat{a}$ or the right-hand side of equation (17) equals zero. A binary search locates the initial value of $\hat{v}$ for which both termination conditions occur simultaneously (i.e., for which the solution passes through the sonic point). The dust fraction must either be small or rapidly decreasing at the sonic point, implying $\tau_d \ll 1$ there (see § 3), so the initial guess of the value of τ_d is adjusted until τ_d is less than a few percent at the sonic point. Usually only one such adjustment is needed.

4.2. *Results*

Figures 4–6 show a representative wind solution with $\hat{r}_{\rm cl} = 5.34 \times 10^{-3}$. As the gas departs from thermal equilibrium at the surface of the cloud, H rises sharply to a few times $H_{\rm C}$. Here there are still some metals left that contribute to the photoionization heating but whose emission lines lie in the few keV range and that are not excited at the $\sim 10^5$ K temperature of the gas. Since both the ionization parameter $\Xi \simeq \Xi^0/\hat{a}^2$ and the temperature rise, soon even these metals are fully ionized, and H approaches $H_{\rm C}$. The sputtering rate rises with the initial rapid increase in temperature and then declines as the temperature levels off and the density decreases. Between the cloud surface and the sonic point, the sputtering rate is substantial ($d \ln \chi_d/d \ln r \sim$ several). As a result the dust fraction drops rapidly to negligible levels and $H/v|\mathscr{F}| \gg 1$, so that the radiation force does not influence the structure of the wind. The optical depth is typically <0.1 between the cloud surface and the sonic point and is no more than a few tenths at the cloud surface.

Figures 7 and 8 show the dependence of $\hat{a}_s$ and $\hat{r}_s$ on $\hat{r}_{\rm cl}$. For $3 \times 10^{-4} < \hat{r}_{\rm cl} < 3 \times 10^{-2}$, the gas is hot, sputtering is efficient, and $v\mathscr{F} \ll H$. Also, $\hat{a}_s \ll 1$ so that $H \simeq H_{\rm C} = $ const. Therefore, for $\hat{r}_{\rm cl}$ in this range $\hat{a}_s \simeq \hat{r}_{\rm cl}^{1/3}$ and $\hat{r}_s \simeq \hat{r}_{\rm cl}$ as derived analytically in §§ 2.3 and 3. For $\hat{r}_{\rm cl} > 3 \times 10^{-2}$, $\hat{a}_s$ approaches

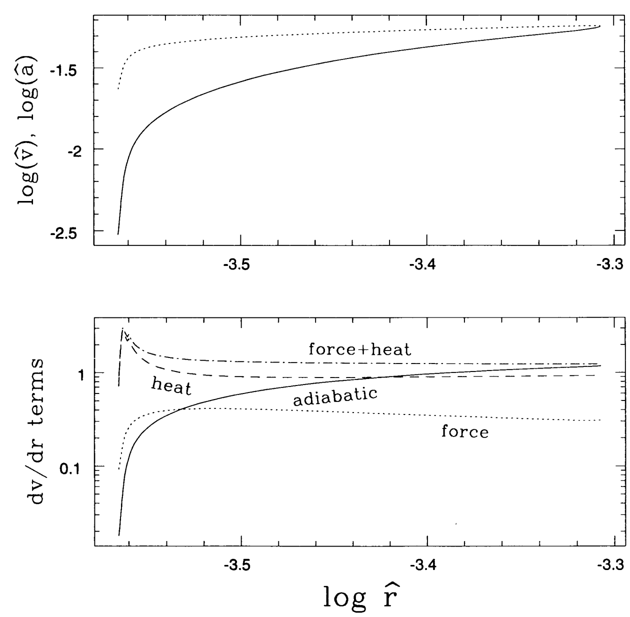

FIG. 4.—Typical wind solution. In the upper panel are plotted $\hat{v}$ (*solid line*) and $\hat{a}$ (*dotted line*) as functions of $\hat{r}$ between the cloud surface and the sonic point. The lower panel shows various terms on the right-hand side of eq. (17). The curve labeled "heat" represents $H/H_{\rm C}$, "force" represents $(3/2)(\mathscr{F} a_{\rm C}/H_{\rm C})\hat{v}$, and "adiabatic" represents $3\hat{a}^2\hat{v}/\hat{r}$. Note that at the sonic point $\hat{v} = \hat{a}$ and the adiabatic term equals the sum of the force and heat terms.

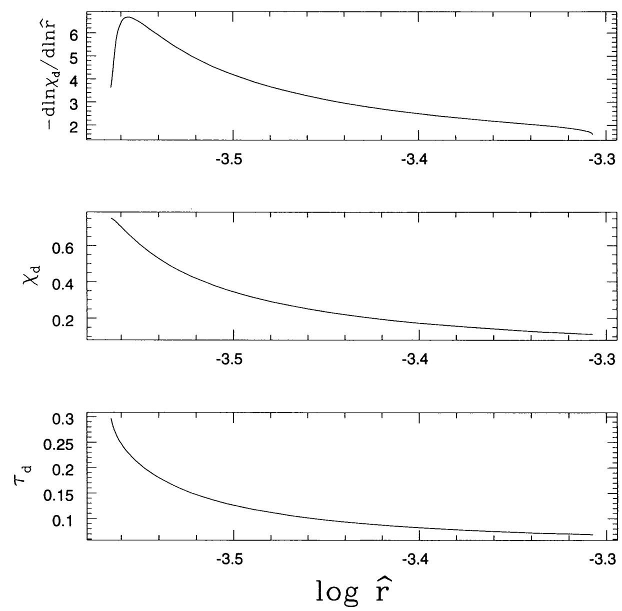

FIG. 5.—Typical wind solution. Plotted are the sputtering rate (*top panel*), the dust fraction (*middle panel*), and the dust optical depth (*bottom panel*).

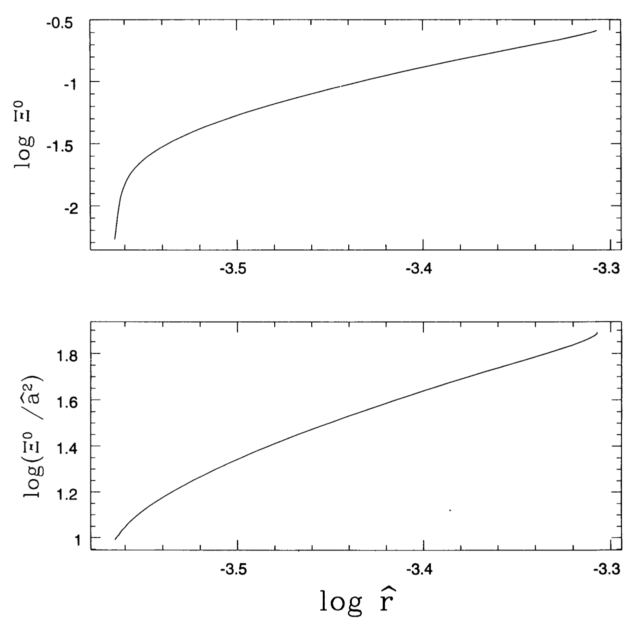

FIG. 6.—Typical wind solution. The upper panel plots Ξ^0 which is inversely proportional to density. The lower panel plots $\Xi^0/\hat{a}^2$ which is approximately equal to Ξ.

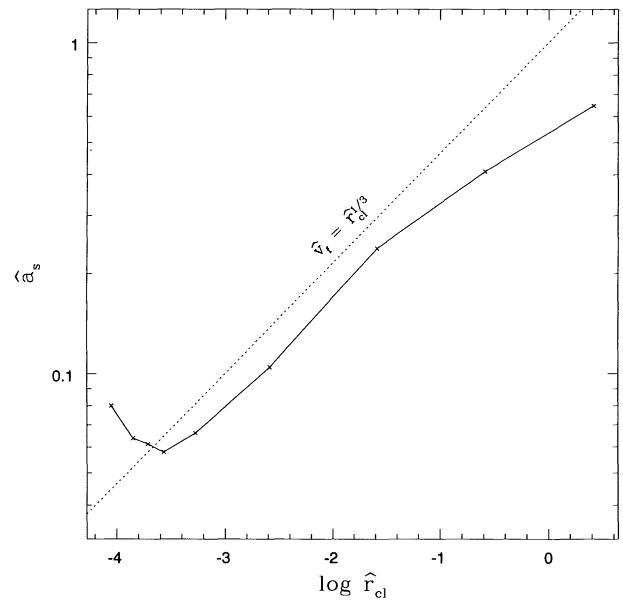

FIG. 7.—Sound speed at the sonic point as a function of $\hat{r}_{cl}$. The dotted line represents the typical velocity scale of the wind derived in § 2.3.

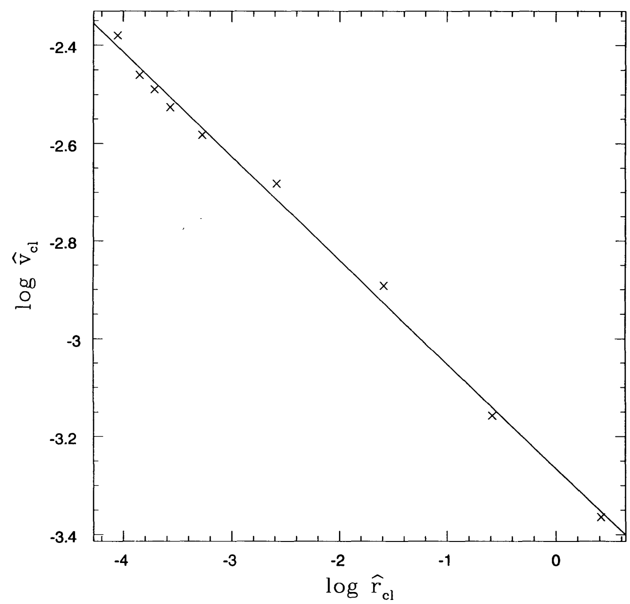

FIG. 9.—Velocity at the cloud surface as a function of $\hat{r}_{cl}$. The points represent model results, and the line represents a least-squares fit with $\hat{v}_{cl} = 5.43 \times 10^{-4} \hat{r}_{cl}^{-0.21}$.

unity asymptotically and H/H_C at the sonic point falls to zero as Compton cooling approaches H_C.

From equations (20) and (23), $d \ln \chi_d / d \ln r \propto \hat{v}_{cl} \hat{r}_{cl}^2 \hat{a}_s^4 / \hat{r}$ at the sonic point for $\hat{a} \ll 0.1$. Since $\hat{v}_{cl}$ is only weakly dependent on $\hat{r}_{cl}$ (Fig. 9) while $\hat{r}_s \propto \hat{r}_{cl}$, the sputtering rate at the sonic point decreases with decreasing $\hat{r}_{cl}$. As the sputtering rate declines, radiation pressure becomes increasingly important. For $\hat{r}_{cl} < 3 \times 10^{-4}$, $H/v|\mathscr{F}| \simeq 2$ through most of the wind. According to equation (17), such a wind passes through a sonic point only if $d \ln \chi_d / d \ln r < -1$ (Fig. 10). While $\hat{a}_s < 0.1$ the strong temperature dependence in equation (23) means that the wind can maintain a high enough sputtering rate by moving its sonic point to higher a_s and larger radii. However, when $\hat{r}_{cl} \lesssim 10^{-4}$, $\hat{a}_s$ reaches 0.1, and the temperature dependence saturates. Then the sputtering rate becomes too low for the flow to pass through the sonic point, and no physical solutions are possible (Fig. 11).

The optical depth at the cloud surface (Fig. 12) decreases with r_{cl} as the sputtering rate increases. Note that $\tau_d(\hat{r}_{cl}) \leq 0.3$ for all $\hat{r}_{cl}$. Therefore, the continuum illuminating the cloud surface is essentially independent of $\hat{r}_{cl}$. Since the cloud is radiation pressure confined, the ionization structure of the cloud is

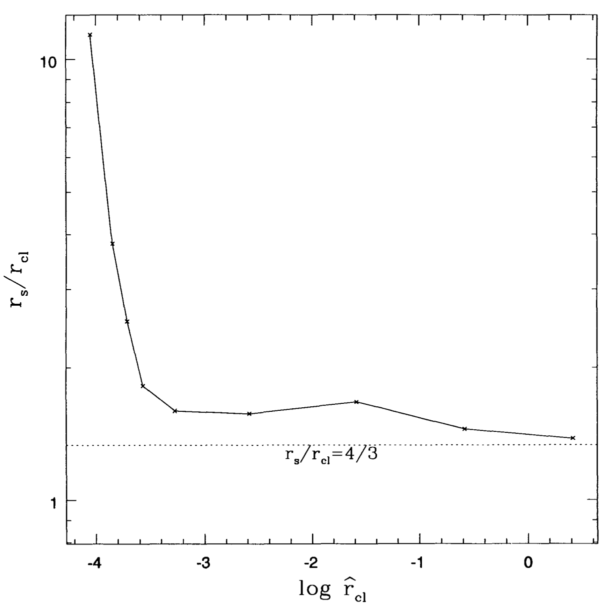

FIG. 8.—Radius of sonic point as a function of $\hat{r}_{cl}$. The dotted line represents the approximate value of r_s derived analytically in § 3.

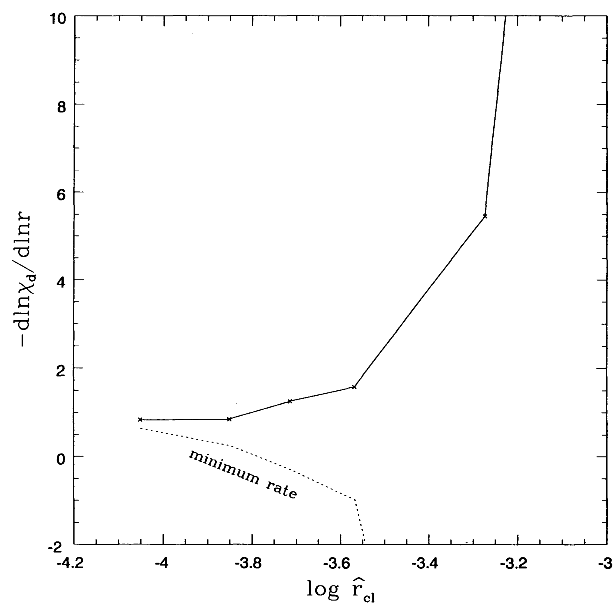

FIG. 10.—Sputtering rate at the sonic point as a function of $\hat{r}_{cl}$. The dotted line represents the minimum sputtering rate for which the wind could pass through the sonic point from eq. (16).

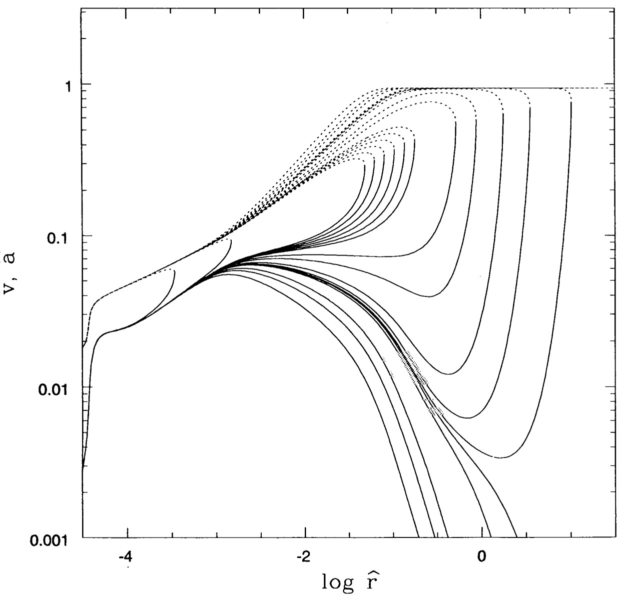

FIG. 11.—Various nonphysical solutions for $\hat{r}_{cl} = 3 \times 10^{-5}$, each one differing in $\hat{v}_{cl}$. For such a small value of $\hat{r}_{cl}$, the radiation force stifles the wind, and no solution passes through the sonic point. The dotted lines represent $\hat{a}$, while the solid lines represent $\hat{v}$.

independent of $\hat{r}_{cl}$. Ionization balance and line emission will be discussed more completely in § 5.

4.3. *Mass Loss*

The mass-loss rate in the wind is $\dot{M} = 4\pi(1.4m_H)n_H vr^2$. In terms of dimensionless quantities,

$$\dot{M} = 4\pi \frac{F_{tot} l_C^2}{ca_C} \frac{\hat{v}\hat{r}^2}{\Xi^0} . \tag{24}$$

From equation (1), $M = (1.12 \times 10^9\ M_\odot)\xi\hat{r}_{cl}^3(F_{tot}/10^7$ ergs cm^{-2} s$^{-1})T_{mol3}^{-1}$. The models give $\hat{v}_{cl} \simeq 5.43 \times 10^{-4} r_{cl}^{-0.21}$ (Fig. 9); hence,

$$\dot{M} = 1.79 \times 10^{-5}\left(\frac{F_{tot}}{10^7 \text{ ergs cm}^{-2} \text{ s}^{-1}}\right)^{0.19} \times \left(\frac{M}{10\ M_\odot}\right)^{0.60} \xi^{0.60} T_{mol3}^{0.60}\ M_\odot \text{ yr}^{-1} . \tag{25}$$

A cloud of mass M then evaporates in a time

$$t_{evap} = 5.57 \times 10^5\left(\frac{F_{tot}}{10^7 \text{ ergs cm}^{-2} \text{ s}^{-1}}\right)^{-0.19} \times \left(\frac{M}{10\ M_\odot}\right)^{0.40} \xi^{0.60} T_{mol3}^{-0.60} \text{ yr} . \tag{26}$$

For comparison, the orbital period of a cloud about the active nucleus is

$$t_{orb} = 2.29 \times 10^3\left(\frac{F_{tot}}{10^7 \text{ ergs cm}^{-2} \text{ s}^{-1}}\right)^{-3/4} \times \left(\frac{L}{10^{11}\ L_\odot}\right)^{1/4}\left(\frac{L/L_{Edd}}{0.01}\right)^{1/2} \text{ yr} , \tag{27}$$

where L is the bolometric luminosity of the active nucleus and L_{Edd} is its Eddington luminosity. Another relevant timescale is the drift time, $t_{drift} = R/v_r$, where v_r is the mean radial velocity of clouds in the torus due to inelastic collisions between clouds and R is the characteristic radius of the torus. If we assume that the material in the torus fuels the active nucleus, then $L = f_{cap}\epsilon c^2 R^2 v_r(1.4m_H \bar{n}_H)\Delta\Omega$, where f_{cap} is the fraction of the torus material which is eventually accreted by the nucleus, ϵ is the efficiency with which the nucleus turns matter into energy $\bar{n}_H$ is the mean hydrogen density of the torus, and $\Delta\Omega$ is the solid angle about the nucleus covered by the torus. This assumption yields

$$t_{drift} = 2.4 \times 10^5\left(\frac{f_{cap}}{0.5}\right)\left(\frac{\epsilon}{0.1}\right)\left(\frac{\Delta\Omega/4\pi}{0.7}\right)\left(\frac{\bar{n}_H R}{10^{24} \text{ cm}^{-2}}\right) \times \left(\frac{F_{tot}}{10^7 \text{ ergs cm}^{-2} \text{ s}^{-1}}\right)^{-1} \text{ yr} . \tag{28}$$

Although equations (26) and (28) involve several poorly known quantities $t_{evap} \sim t_{drift}$, as must be the case if cloud evaporation determines the inner edge of the torus. This supports our choice of $F_{tot} \sim 10^7$ ergs cm^{-2} s^{-1} and the inner edge effective temperature $\sim$600 K found by Pier & Krolik (1993). On the other hand, $t_{orb} \ll t_{evap}$. Therefore, clouds on highly eccentric orbits approach the nucleus much more closely than those on circular orbits. This is consistent with infrared observations which indicate that a small amount of $\sim$1500 K dust is present well inside the inner edge of the torus (Pier & Krolik 1993; Ruiz, Rieke, & Schmidt 1994).

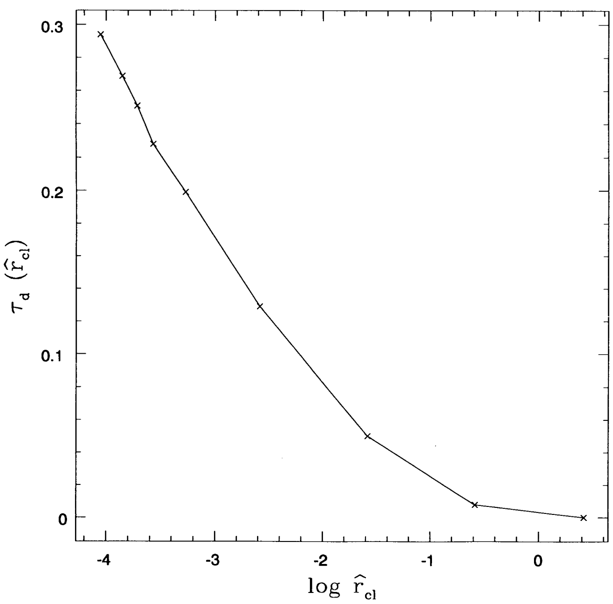

FIG. 12.—Dust optical depth at the cloud surface as a function of $\hat{r}_{cl}$. Note that the wind is optically thin for all $\hat{r}_{cl}$ for which a physical spherical wind solution exists.

5. STATIC, LINE-EMITTING CLOUD

The spectra of AGNs exhibit emission lines coming from at least two distinct regions. The narrow-line region (NLR) has low density ($n_H \sim 10^5$), moderate ionization ($\Xi \lesssim 1$), and a velocity dispersion of a few hundred km s^{-1}. The broad-line region (BLR) has high density ($n_H \gtrsim 10^9$), possibly higher ionization, and a velocity dispersion of several thousand km s^{-1}. Some AGNs also show forbidden lines from high-ionization stages of iron such as [Fe VII] λ6087, [Fe X] λ6375, [Fe XI] λ7892, and [Fe XIV] λ5303, known collectively as "coronal lines" (Korista & Ferland 1989). They require Ξ of several and $n_H \lesssim 10^7$–10^{10} cm^{-3} (so that they will not be collisionally de-excited) and have line widths intermediate between those of the broad and narrow lines. The coronal lines are therefore not easily produced in either the NLR or BLR. The clouds on the inner edge of the torus provide a natural place to produce these lines since $n_H \sim 10^8$ cm^{-3} and $\Xi \simeq \Xi_{cr}$ near their surfaces. However, the torus must not produce fluxes of recombination lines such as Hα and Hβ or forbidden lines such as [O III] λ5007 stronger than those we see coming from the NLR and BLR. This is a significant constraint since the torus is thought to cover a much larger fraction of the solid angle about the nucleus than either the NLR or BLR. The models we present here can account for both the production of the coronal lines and the relative weakness of other emission lines from the torus.

We have calculated the line emission from a cloud on the inner edge of a torus using Timothy Kallman's photoionization code XSTAR (Kallman & Krolik 1993). This code was modified to include dust extinction and coronal line emission. Dust absorption was added to the gas opacity to calculate the attenuation of the incoming continuum and the line probabilities. We used the Draine & Lee (1984) extinction curve but ignored scattering. The coronal line data were the same as those used by Korista & Ferland (1989). We modeled the line-emitting layer of the cloud as a plane-parallel slab, illuminated by a source at a great distance from the surface. Since $\tau_d < 1$ through the wind for all $\hat{r}_{cl}$ (see § 4) we take the illuminating flux to be F_ν^0, with $F_{ion} = 10^7$ ergs cm^{-2} s^{-1}. Since $\Xi < \Xi_{cr}$ and $v \ll a$ below the surface of the cloud, we set $H = 0$ and $P_g + P_{rad}$ = const, where P_{rad} is the local radiation pressure. We take $\chi_d = 1$ throughout the cloud.

Note that since $P_{rad}/P_{gas} = \Xi_{cr}$ at the surface of the cloud, the ionization structure of the cloud depends only on the incident spectral shape and the opacity in the cloud. Therefore, barring strongly atypical ionizing continua or cloud compositions, all evaporating clouds will produce essentially the same emission line spectra.

Figure 13 shows Ξ, n_e/n_H, and T as functions of τ_d in the cloud. As τ_d goes from 0 to 1, Ξ drops rapidly from Ξ_{cr} to unity and T drops to $\lesssim$30,000 K. As τ_d increases beyond 1, Ξ drops much more gradually since most of the incident UV radiation has been absorbed and the frequency-averaged opacity is much less. Both hydrogen and helium are fully ionized for $\tau_d < 3$. At this point He II becomes dominant over He III. At $\tau_d \simeq 4$ hydrogen becomes neutral and n_e drops to $0.1n_H$.

The line fluxes from our model clouds are generally very low. In particular, $F(\mathrm{H}\alpha) = 3.6 \times 10^{-3}F_{ion}$, $F(\mathrm{H}\beta) = 3.8 \times 10^{-4}F_{ion}$, and F(O III λ5007) $= 8.3 \times 10^{-5}F_{ion}$. Typical dust-free NLR models give line fluxes an order of magnitude or more larger. The clouds on the inner edge of the torus are inefficient line emitters for three reasons. First, the gas on the surface of the cloud is highly ionized and relatively transparent to the incident radiation, so most of the incident ionizing energy is absorbed directly by dust grains and reradiated in the infrared. Second, lower ionization gas is hidden behind a screen of dust which absorbs the outgoing lines. Third, when $n_H \sim 10^8$ cm^{-3}, many of the usual forbidden lines (e.g., [O III] λ5007) are collisionally de-excited. Because of reddening, our model predicts $F(\mathrm{H}\alpha)/F(\mathrm{H}\beta) = 9.4$, much larger than value of 3.0 predicted by case B recombination.

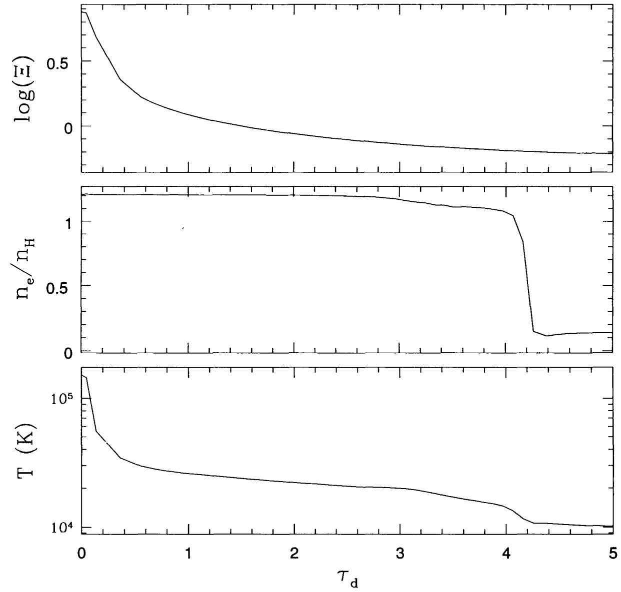

FIG. 13.—Ionization parameter, electron density, and temperature below the surface of the cloud.

The ratio between the coronal line fluxes and the fluxes of the permitted lines and the C, N, and O forbidden lines is higher in evaporating clouds than in the NLR. This is true for two reasons. First, the evaporating clouds have a highly ionized region in which the coronal lines may be produced. Second, that region is at a low optical depth so that the coronal lines may easily escape the cloud. Therefore, the torus can provide the coronal line fluxes observed in Seyfert galaxies without overproducing the other emission lines. Table 1 compares the line fluxes from our photoionization models with the line fluxes observed in Seyfert 2 galaxies. We have scaled the lines relative to [Fe X] λ6375 in order to illustrate that the coronal lines themselves are produced in roughly the right

TABLE 1

SELECTED LINE FLUXES RELATIVE TO [Fe X] λ6375

Line	Cloud Model[a]	Average Seyfert 2[b]	NGC 1068[c]
Hα	46.0	78	95.0
Hβ	4.9	25.0	21.0
Lyα	69.0	1400	135.0
C III λ997	2.8	...	10.0
C III] λ1909	17.0	140	32.0
C IV λ1549	110	300	52.8
N IV] λ1487	5.0	...	6.8
[O III] λ5007	1.1	270	280
O VI λ1034	64.0	...	49.7
[Fe VII] λ6087	0.64	2.5	4.7[d]
[Fe XI] λ7892	0.63	...	1.5
[Fe XIV] λ5303	0.18	...	...
Mg II λ2798	7.9	45.0	17.0

[a] $F_{6375} = 7.8 \times 10^{-5} F_{ion}$ for the model.
[b] Average Seyfert 2 galaxy spectrum compiled by Ferland & Osterbrock 1986.
[c] Optical lines from Koski 1978, UV lines with λ < 1800 Å from Kriss et al. 1992, and with λ > 1800 Å from Snijders, Netzer, & Boksenberg 1986. $F_{6375} = 7.52 \times 10^{-14}$ ergs cm^{-2} s^{-1}.
[d] May be blended with [Ca V] λ6087.

proportions and that no other lines are overproduced. In the models, the C IV/[Fe X] and O VI/[Fe X] line ratios are slightly larger than those observed in NGC 1068; however, a small amount of foreground dust extinction would attenuate the UV lines to within reasonable levels, and the coronal line atomic data are accurate only to within a factor of 2 (Korista & Ferland 1989).

The widths of the coronal lines from the inner edge of a torus would be dominated by the random and orbital motions of the clouds. We therefore expect linewidths of order

$$v_{\rm orb} = 1300\left(\frac{L/L_{\rm Edd}}{0.01}\right)^{-1/2}\left(\frac{L}{10^{11}\,L_\odot}\right)^{1/4} \times \left(\frac{F_{\rm tot}}{10^7 \text{ ergs cm}^{-2}\text{ s}^{-1}}\right)^{1/4} \text{km s}^{-1}\,. \quad (29)$$

Such widths are similar to those observed.

The coronal line luminosity from the torus is proportional to the solid angle about the nucleus covered by the torus, $\Delta\Omega$, and the fraction of the inner edge which is visible, $f_{\rm vis}$. If we take the observed ionizing flux for NGC 1068 to be $8.7 \times 10^{-9} f_{\rm refl}^{-1}$ ergs cm^{-2} s^{-1} as determined by Pier et al. (1994) (where $f_{\rm refl} \sim 10^{-2}$ is the fraction of the nuclear flux which is scattered into our line of sight), then the torus will produce the observed [Fe X] λ6375 flux if $f_{\rm vis} = 0.14[(\Delta\Omega/4\pi)/0.8](f_{\rm refl}/10^{-2})$. We have scaled $\Delta\Omega$ to the value for the observed opening angle of the ionization cone in this galaxy (Evans et al. 1991).

6. SUMMARY

We have shown that the UV/X-ray continuum of an AGN can drive a thermal wind from the surface of a dusty molecular cloud. Dust grains from the cloud will be carried along with the wind and will be destroyed by sputtering in the hot ($T \geq 10^6$ K) gas when $r_{\rm cl} > (2 \times 10^{15}\text{ cm})T_{\rm C8}^{1/2}F_7^{-1}(F_{\rm ion}/F_{\rm tot})$, corresponding to $M > (0.2\,M_\odot)T_{\rm C8}^{3/2}(F_{\rm ion}/F_{\rm tot})^3F_7^{-2}T_{\rm mol3}^{-1}$. If this condition is not met, radiation forces on the dust grains will strongly affect the flow. When radiation pressure is unimportant, the cloud evaporates completely in $t_{\rm evap} = 5.57 \times 10^5(F_7\,F_{\rm tot}/F_{\rm ion})^{-0.19}(M/10\,M_\odot)^{0.40}T_{\rm mol3}^{-0.60}$ yr. If we assume that torus material drifts inward at the rate needed to fuel the active nucleus, the resulting drift time is comparable to this evaporation time. Evaporation may be responsible for setting the inner radius of the torus, but $t_{\rm evap}$ is much greater than the orbital period of the torus enabling clouds on eccentric orbits to penetrate well inside this inner radius. In our spherically symmetric models, radiation forces suppress the outflows from small clouds, but the models are invalid in this limit. When radiation forces are important, ablation, rather than evaporation, is likely to dominate the removal of matter from the cloud.

The inner faces of torus clouds exposed to the AGN flux are pressurized primarily by the incident radiation; thus, their gas pressure increases with optical depth. While the bulk of the cloud is molecular and largely neutral, there is a surface layer of ionized gas with $n_{\rm H} \sim 10^8 F_7$ cm^{-3}. Dust in this layer absorbs most of the ionizing radiation incident upon the cloud, so recombination lines are produced ineffeciently. This explains how tori with high covering factors manage to remain relatively dim in recombination-line flux. The combined effects of dust extinction and high density suppress most of the usual lines seen in AGN spectra, but evaporating clouds quite naturally produce the coronal lines from highly ionized iron. These lines are often seen in AGN spectra but are not easily generated in either the NLR or BLR. Our models can account for the observed coronal line fluxes, and the observed coronal line widths ($\sim$1000 km s^{-1}) coincide with the orbital velocities expected on the inner edge of an obscuring torus.

The authors thank Timothy Kallman and Julian Krolik for helpful discussions. This work was supported by NASA through grant HF-1054.01-93 from the Space Telescope Science Institute, which is operated by the Association of Universities for Research in Astronomy, Inc., under NASA contract NAS 5-26555.

REFERENCES

Antonucci, R. R. J. 1993, ARA&A, 31, 473
Antonucci, R. R. J., & Miller, J. S. 1985, ApJ, 297, 621
Balsara, D., & Krolik, J. H. 1993, ApJ, 402, 109
Begelman, M. C., McKee, C. F., & Shields, G. A. 1983, ApJ, 271, 70
Bondi, H. 1952, ApJ, 112, 195
Draine, B. T., & Lee, H. M. 1984, ApJ, 285, 89
Draine, B. T., & Salpeter, E. E. 1979, ApJ, 231, 77
Edelson, R. A., Malkan, M. A., & Rieke, G. H. 1987, ApJ, 321, 233
Evans, I. N., et al. 1991, ApJ, 369, L27
Ferland, G. J., & Osterbrock, D. E. 1986, ApJ, 300, 858
Kallman, T. R., & Krolik, J. H. 1993, XSTAR: A Spectral Analysis Tool: A Brief Description (NASA internal report)
Kay, L. E. 1994, ApJ, 430, 196
Korista, K. T., & Ferkand, G. J. 1989, ApJ, 343, 678
Koski, A. T. 1978, 223, 56
Kriss, G. A., et al. 1992, ApJ, 394, L37
Krolik, J. H., & Begelman, M. C. 1986, ApJ, 308, L55
———. 1988, ApJ, 329, 702
Krolik, J. H., & Lepp, S. 1989, ApJ, 347, 179
Krolik, J. H., McKee, C. F., & Tarter, C. B. 1981, ApJ, 249, 422
Laor, A., & Draine, B. T. 1993, ApJ, 402, 441
Lawrence, A. 1991, MNRAS, 252, 586
Macchetto, F., Capetti, A., Sparks, W. B., Axon, D. J., & Boksenberg, A. 1994, ApJ, 435, L15
Mathis, J. S., Rumpl, W., & Nordsieck, K. H. 1977, ApJ, 217, 425
Miller, J. S., & Goodrich, R. W. 1990, ApJ, 355, 456
Morrison, R., & McCammon, D. 1983, ApJ, 270, 119
Mulchaey, J. S. 1994, Ph.D. thesis, Univ. of Maryland
Netzer, H., & Laor, A. 1993, ApJ, 404, L51
Neufeld, D. A., Maloney, P. R., & Conger, S. 1994, ApJ, 436, L127
Pier, E. A., Antonucci, R., Hurt, T., Kriss, G., & Krolik, J. 1994, ApJ, 428, 124
Pier, E. A., & Krolik, J. H. 1993, ApJ, 418, 673
Pogge, R. W. 1988, ApJ, 328, 519
———. 1989, ApJ, 345, 730
Ruiz, M., Rieke, G. H., & Schmidt, G. D. 1994, ApJ, 423, 608
Sanders, D. B., et al. 1989, ApJ, 325, 74
Schmitt, H. R., Storchi-Bergmann, T., & Baldwin, J. A. 1994, ApJ, 423, 237
Snijders, M. A., Netzer, H., & Boksenberg, A. 1986, MNRAS, 222, 549
Spitzer, L. 1978, Physical Processes in the Interstellar Medium (New York: Wiley)
Storchi-Bergmann, T., Mulchaey, J. S., & Wilson, A. S. 1992, ApJ, 395, L73
Tran, H. D., Miller, J. S., & Kay, L. E. 1992, ApJ, 397, 452
Voit, G. M. 1992, ApJ, 399, 495
Ward, M. J. 1994, in Proc. of the Oxford Astrophysics Workshop, Evidence for the Torus, ed. M. J. Ward, in press
Wilson, A. S., Ward, M. J., & Haniff, C. A. 1988, ApJ, 334, 121